Published in final edited form as:
J Geophys Res Planets. 2019 November ; 124(11): 3063–3081. doi:10.1029/2019je006044.

The Seismic Signatures of Recently Formed Impact Craters on Mars

N. C. Schmerr[1], **M. Banks**[2], **I. Daubar**[3]

[1]University of Maryland, College Park.

[2]NASA Goddard Space Flight Center.

[3]Jet Propulsion Laboratory, California Institute of Technology.

Abstract

We investigated the seismic signatures of recent impact crater clusters on Mars that would be recorded by the Interior Exploration using Seismic Investigations, Geodesy and Heat Transport (InSight) seismometers. We used a database of 77 measured and dated impact sites, with craters with diameters between 2.1 and 33.8 m, along with inferred impact angle, bolide trajectory, and varying target material properties to empirically scale for the momentum, expected seismic source function, and radiation pattern of impacts. The impact source is simulated in a local 3-D finite difference wave propagation code and coupled to teleseismic distances by scaling the spectra of 1-D global synthetic seismograms. We use the InSight seismometer noise floors to estimate detectability of impact(s) across azimuth and distance. Our experiments reveal that impact clusters have a higher peak corner frequency resulting from energy contributed by smaller craters to the power spectrum. We also find that the time separation between individual impacts in a cluster is small (< 10–15 milliseconds) and a require a seismometer closely situated to the source (< 10 km) and a high sampling rate (> 100 Hz) to resolve individual impacts within the cluster. Two of the clusters in our database (> 20 m effective diameter) would have been detectable by InSight, with the assumptions that the martian background noise and seismic attenuation are both low. Joint detection of surface changes from newly formed crater(s) in images and by InSight will provide precise source locations that are crucial for constraining the internal structure of Mars.

Plain Language Summary

The recent deployment of a seismometer on Mars by the NASA mission InSight creates the possibility that we will be able to detect the ground motions produced by rocks and other debris from space hitting the surface of the red planet and creating impact craters. Mars is still being cratered today, with about half of the recently formed impacts observed to occur in tightly spaced scattershot-like clusters, with the incoming object presumably fragmenting in the atmosphere before impact. By finding the location of the resulting crater(s) in images and associating them with a particular seismic event recorded by InSight, we can establish the precise location of the resulting marsquake. Here we studied the expected seismic signatures of these recent impact crater clusters to determine how detectable they would be by InSight's sensitive seismometers. Our experiments show that crater clusters are louder than a singular impact and release more energy at

Corresponding author: Nicholas Schmerr (nschmerr@umd.edu).

higher frequencies than individual craters. Of the clusters we studied, at least two would have been detectable by InSight above the background environmental noise of Mars. Ultimately these impact signals will be invaluable for studying the martian interior and learning more about the impact cratering process itself.

1 Introduction

Impact cratering is a fundamental process that drives the surface evolution of objects throughout the Solar System. Nearly every solid surface shows evidence for extensive impact cratering in the geological record, and the abundance of impact craters at varying sizes has become a basic tool for judging the relative ages of surfaces throughout the Solar System (Melosh, 1989). Despite the wealth of craters, opportunities to directly observe the physics involved in the processes of bolide impact, crater excavation, ejecta deposition, and subsequent collapse of the target materials have primarily been limited to laboratory experiments (e.g., Holsapple et al., 2002), a small number of recordings of bolide impacts on Earth (Edwards et al., 2008), and artificial and natural impacts recorded during the Apollo seismic experiment (Toksoz, 1974).

The landing of the Interior Exploration using Seismic Investigations, Geodesy and Heat Transport (InSight) mission and deployment of the Seismic Experiment for Interior Structure (SEIS) short period (SP) and very-broad-band (VBB) seismometers (Banerdt et al., 2017) in late 2018 on Mars gives us a new opportunity to observe seismic waves generated by the impact process in-situ at another terrestrial planet. Newly formed and recent impact craters on Mars and the Moon have been identified through a variety of methods, both directly and indirectly. Direct techniques include repeat high resolution imaging of the planetary surface revealing the occurrence of newly formed craters (Daubar et al., 2014b) and/or albedo changes associated with impact cratering (Speyerer et al., 2016), the excavation or stripping of dusty surface veneers in the vicinity of a fresh-looking impact crater (Malin et al., 2006), and observations of impact flashes in telescopes (Ortiz et al., 2006). Indirect techniques include detection of seismic waves excited by the impact in the target materials (Davis, 1993), acoustic detection of the bolide traveling in the atmosphere (Popova et al., 2003), or atmospheric disruptions of the cloud layer of gas giants (Harrington et al., 1994). Identification of fresh, recent impact craters is essential for understanding the current flux of bolides in the Solar System, and the rate of impact cratering on modern surfaces (Daubar et al., 2013).

This flux of bolides represents an important potential source of seismicity for past and future geophysical missions in the Solar System. As an example, over 3000 individual impact events were detected by the four seismometers placed on the Moon by the Apollo astronauts (Nakamura et al., 1982), as well as artificial impacts of the Stage IV-B of the Saturn V rockets and Lunar landing modules (Latham et al., 1970a). Given the paucity of shallow tectonic moonquakes (Nakamura et al., 1974), lunar impact events were fundamental for calibrating the response of the Apollo seismic array (Lammlein et al., 1974), and essential data points for inversions for lunar internal structure (Nakamura et al., 1982). The InSight mission to Mars (Banerdt et al., 2017) is expected to be able to observe martian impacts

(Teanby & Wookey, 2011). For a low martian noise model, (Teanby & Wookey, 2011) predicted the detection of at least 1 impact event per year at less than 60° epicentral distance from the station, and (Teanby, 2015) refined this to 1–3 impact events per year at regional distances (< 20°) assuming an instrumental noise floor of 10^{-8} $ms^{-2}Hz^{-1/2}$. Indeed, recent efforts by Daubar et al., (2016) have identified over 400 newly formed and dated impact craters in the dusty equatorial regions of Mars, suggesting there is high likelihood InSight will detect an impact during the nominal mission lifetime of 2 Earth years or greater.

Our project, IMPACT-SEISM (Investigating the Morphometric Properties of All-New Craters and the Transfer of Seismic Energy from Impacts into the Subsurface of Mars), presents new measurements of crater morphometry for recent (< 20 years old) dated impact clusters on the surface of Mars (Daubar et al., 2019), and uses a seismological model to predict the detectability and seismic character of impacts at Mars (Figure 1). This catalog of young dated impacts builds upon the past efforts presented in Daubar et al., (2013) and expands the database with 77 new crater locations on Mars. We connect the observed crater(s) to a seismic source magnitude by a scaling law relating crater diameter to the momentum imparted by the bolide to the target. By modeling the amplitudes of surface and body waves of the impact source, we can investigate how to identify impact seismicity, and how it will inform on the internal structure of Mars. Ideally, identification of impact craters in future mission deployments similar to InSight would lead to a search for the fresh crater(s) in visible images taken from orbit, providing a precise spatial control on the source location and making impact events invaluable for structural inversions of seismic data where source locations are typically poorly known. Our coupled impact-seismic model is generalizable to other bodies for which we have measurements of impact morphologies and seismic observations.

2 Crater Database Description

Our crater database is drawn from Daubar et al., (2019) where we measured the morphometries of 77 dated impact sites in images from the High Resolution Imaging Science Experiment (HiRISE) on the Mars Reconnaissance Orbiter (MRO) spacecraft (McEwen et al., 2007). The smallest crater that we include into our dataset is 1 meter in diameter, although craters smaller than this size are identifiable in the highest resolution HiRISE images (up to 25 cm per pixel), their crater rims are not clearly resolved. We selected 1 meter as the cutoff size as it becomes more difficult to distinguish secondary and pre-existing craters from the primary craters at smaller sizes. Secondly because the seismic source associated with smaller crater formation is not likely detectable > 1 km from impact. Previous studies by Daubar et al., (2013) report that 56% of dated recent impacts form as clusters of two or more individual craters, with clusters being more detectable than single craters due to the increased size of the area darkened by removal of surface dust. Likewise, detection of new dated impacts is primarily limited to regions with considerable dust, so the population of craters reported here is very likely an undersampling of the true impact rate of Mars. We measured the size, geographical dispersion, and ellipticity of the crater distribution in crater clusters, using these parameters to infer the direction and angle of impact. Here we use these parameters to approximate the temporal and spatial distribution of seismic sources as the cluster forms. Note that we do not specifically address the atmospheric seismic

signatures of these impacts, which may contain information about the timing, modification, and breakup of bolides as they traverse the atmosphere (Collins et al., 2017; Ivanov et al., 2009; Karakostas et al., 2018; Popova et al., 2007; Stevanovic et al., 2017; Williams et al., 2014). Here we report on the expected ground motion signature and detectability of these impact crater clusters, with implications for the future detectability of impacts by the InSight seismometers on Mars.

3 Impact Source Model

There exist a variety of different methods for approximating the impact source, including scaling laws derived from explosive and low-velocity impacts (Teanby & Wookey, 2011), treatment of the source as a momentum transfer (Gudkova et al., 2014; Lognonne et al., 2009), hydrodynamic simulations of particle motions and stress (Güldemeister & Wünnemann, 2017; Ivanov & Artemieva, 2002), and permanent volume injection (Richardson et al., 2005). To study the predicted amplitudes of seismic waves generated by impacts, we have adopted a model in which the momentum transfer is calibrated by lunar impact observations from Apollo (Lognonne et al., 2009) and captures the inherent frequency dependence of an impact seismic source. Impacts are treated as an inefficient transfer of momentum to the target volume, where the source excitation function I (momentum) is described by the integrated force f(t) applied across some impulse of duration τ (in seconds).

$$\mathrm{I} = \int_0^{\tau} \mathrm{f}(t)dt \qquad \text{Eq. 1}$$

We derive the source duration τ of an impact from an empirical power law relating the momentum of artificial and natural impacts and source durations observed at the Apollo seismic stations on the Moon (Gudkova et al., 2011).

$$\tau = 0.65\left(\frac{I}{10^7}\right)^{0.14} \qquad \text{Eq. 2}$$

As few large impacts were observed during Apollo, this relationship is appropriate for smaller impacts and becomes less certain at larger values of I (Gudkova et al., 2011). The source duration τ is presumably related to the characteristic decay time of the initial shock wave, crater modification period, and deposition of ejecta. Our crater database of individual crater diameters ranges from 1 meter to up to 24.8 m, comparable to the range of impact craters detected by the Apollo seismic experiments (Gudkova et al., 2011). A similar empirical relationship for martian impacts may be measured by InSight, but remains presently unavailable, so we adopt lunar values for this study.

During an impact, there will be losses of energy to fracturing and damaging of the target materials, ejecta removed from the crater, and conversion of energy to heat, with the resulting seismic amplitudes being a function of the efficiency of all these processes. A perfectly inelastic impact will transfer all momentum to the target body, while a perfectly elastic impact will double the imparted momentum as it rebounds from the target. The

removal of ejecta can increase this efficiency beyond 2 or greater (McGarr et al., 1969). Experiments with a wide variety of materials show that the resultant seismic amplification varies widely, ranging from a value of 1–2 in sand, to higher values in bonded or solid media (Holsapple, 1993; McGarr et al., 1969). To quantify this effect, Lognonné et al., (2009) used the impact model of (Holsapple, 1993) to estimate the mass and velocity of the ejecta for a rocky bolide into lunar regolith, and then found the total momentum imparted into the ejecta by integration across ejecta velocity and mass. They fit a power law to their integrated results for different bolide velocities and found the following relationship between the momentum imparted by the bolide I to the expected momentum of the ejecta, p_{ejecta}:

$$S = \frac{I}{mv} = 1 + \frac{p_{ejecta}}{mv} = 1 + \eta\left[\frac{v}{v_0}\right]^{0.22} \quad \text{Eq. 3}$$

Where m is the mass (kg), v the velocity of the bolide (km/s), v_0 a reference velocity of 1 km/s, η is the ejecta contribution coefficient, and S is the non-dimensional seismic amplification factor (Gudkova et al., 2011). For Eq 3., the value of η is dependent upon impactor density and impact angle; this value ranges from 0.02–0.70 for the Apollo recorded lunar impacts. Here we assign a value of 0.63 used by (Lognonne et al., 2009). We note that this value may be different for the population of martian impactors and target materials, and that scaling for the transfer of momentum from ejecta is dependent upon factors including impact angle, velocity, target porosity, and strength (Cheng et al., 2016; Holsapple, 1993), all of which affect S. We investigate martian bolide velocity values of 6.5 and 11.5 km/s presented in JeongAhn and Malhotra (2015), who derived these values from their model for the inclination distribution of objects crossing Mars orbit. The seismic amplification is also dependent upon the impact angle; Lognonné et al., (2009) used the power law in Eq. 3 to estimate the effect of the impact angle ψ_v, defined here as the angle from the vertical for a vertically incident impact, as:

$$S(v, \psi_v) = \sqrt{1 + 2\eta \times 0.57\left[\frac{v}{v_0}\right]^{0.22}\cos\psi_v + \left(\eta \times 0.57\left[\frac{v}{v_0}\right]^{0.22}\right)^2} \quad \text{Eq. 4}$$

Eq. 4 makes several implicit assumptions. First, it specifies an ejecta angle of 35°; if we modify the ejecta angle to the more commonly cited value of 45° (Anderson et al., 2004), the resulting estimate for S increases a by ~4% for η=0.63 and becomes negligible for lower values of η. Second, it is assumed the azimuthal distribution of ejecta is isotropic and that ejecta angle is invariant with direction, thus only the vertical component of the net momentum vector is added to the seismic force, as the horizontal components of ejecta momentum cancel each other out. For asymmetric ejecta distributions, there would be an additional horizontal component of momentum pointing in the uprange direction (the opposite direction to the ejected momentum) that is not accounted for here. With those caveats, following Lognonné et al., (2009), and assuming an ejecta angle of 35° and isotropic azimuthal distribution of ejecta, the net seismic force incidence angle for the impact and ejecta, ψ_I, is given by:

$$\cos\psi_I = \frac{\cos\psi_v + \eta \times 0.57\left[\frac{v}{v_0}\right]^{0.22}}{S(v,\psi_v)} \quad \text{Eq. 5.}$$

From Eqs. 4 and 5, and our measured crater properties, we then have the necessary relationships to derive the seismic amplification and seismic force incidence angles required to compute the source time functions for our impact simulations (Fig. 2).

As described in Daubar et al., (2019), Section 2, and reported in Supplemental Tables 1 and 2 of that paper, we independently measure the impact angle ψ_V using the orientation of the ellipsoid that best fits the distribution of craters in our clustered impact database. The horizontal orientation of this ellipsoid also provides the incoming impact azimuth ϕ_I, (with 180° uncertainty), while the ratio of the minor (R_1) and major axes (R_2) is used to compute $\psi_V = \cos^{-1}(R_1 / R_2)$. To resolve the azimuthal uncertainty, we examined the position of the largest crater relative to the best-fit ellipse center, as well as the positions of the top quartile (largest 25%) of craters in the cluster. If the largest crater(s) fell east of the center, the azimuth was taken to be between 0°−180° (*i.e.*, the impactor was traveling westward); if the largest crater fell west of the center, the azimuth was taken to be between 180°−360° (*i.e.*, the impactor was traveling eastward). We could not determine these parameters for singular impacts and clusters with less than 5 craters, so we assumed $\psi_V = 45°$ (the geometrically most common incoming impact angle (Shoemaker, 1961)) and an azimuth $\phi_I = 90°$ to calculate the impact source. Excluding the sites with < 5 craters (n=22), the average impact angle in our cluster database was 62° (n=55).

Seismic amplification relates to another parameter often described in impact experiments, called the seismic efficiency, k, which describes the partitioning of impact energy into seismic energy (Latham et al., 1970b; McGarr et al., 1969; Patton & Walter, 1993; Teanby & Wookey, 2011; Walker, 2003). Seismic efficiency is defined by the seismic energy of an impact ratioed to the bolide kinetic energy, and ranges over a large span of values from k=10^{-2} to 10^{-6} (Richardson et al., 2005). High seismic efficiencies (k> 10^{-3}) are evident in explosions and nuclear tests conducted in highly consolidated materials like bedrock (e.g., Patton & Walter, 1993). Low seismic efficiencies (k< 10^{-5}) are found in sediments, unbounded sands, or regolith and soils (Latham et al., 1970b; McGarr et al., 1969). The approximation of an impact with a nuclear or chemical explosion does not replicate all of the processes involved in a high velocity impact that are driven by a momentum transfer source mechanism. For Mars, a value of ~5×10^{-4} is preferred here based on experiment and theory (Daubar et al., 2018). Based upon Apollo observations of seismic waves generated by artificial and natural impacts, Gudkova et al., (2011) found a seismic efficiency of 10^{-4} to 10^{-5} for lunar impacts, in relatively good agreement with the explosive source estimates for poorly consolidated surface materials (10^{-5}).

Together, equations 1–5 allow us to formulate from a bolide's mass and velocity, the impact momentum I, a source duration τ, and to determine the amplification factor S for the impacts that we observe in our dataset. With these parameters, we then specify a source time function for an impact occurring at time t=0 and location $\vec{x}_s$:

$$I(t) = Sm\overrightarrow{v} * g(t)$$
$$g(t) = \begin{cases} 1 + \cos\omega_1 t \ \text{ for } -\pi/\omega_1 < t < \pi/\omega_1 \\ 0 \qquad\qquad\qquad \text{otherwise} \end{cases} \quad \text{Eq. 6}$$

The value of $\omega_1 = 2\pi/\tau$ and determines the frequency dependence of the source on the impact duration. This source time function is dependent upon the bolide momentum, seismic amplification (Eqs. 3 and 4, seismic efficiency and target properties), impact source duration, and geometry of the impact. This is the same source function used in Gudkova et al., (2015) to describe lunar impacts detected on the Apollo instruments. For the clustered impacts, the time separation between individual impact sources is determined via the distance between craters along the downrange azimuth, and horizontal component of velocity (sine of the bolide incidence angle) assuming two separate velocity values of 6.5 and 11.5 km/s appropriate for Mars (JeongAhn & Malhotra, 2015). These time separations would increase if the bolide decelerates during fragmentation in the atmosphere. The first impact is assigned time zero, and subsequently downrange impacts occur in sequence. The average source time separation is 17 milliseconds (6.5 km/s) and 9 milliseconds (11.5 km/s), with up to 160 milliseconds of source time delay for the most dispersed clusters in our database; see also (Daubar et al., 2019) for calculation of typical time separations. For a purely vertical impact (including those clusters where we were not able to robustly estimate the angle of impact, and all single-crater impacts), the impacts are all assigned the same origin times.

Our next step is to relate the diameter of the observed crater produced by the impact to the impact momentum. Impact crater scaling relationships show that the final radius of the crater is dependent upon the strength and density of the target materials, the gravitational field, impactor momentum (related to velocity, impactor density, and volume), and that there is a tradeoff between gravity driven and strength driven morphologies (Holsapple & Housen, 2012). Here we adopt the crater scaling relationships of Holsapple and Housen (2007) relating the radius of the final crater R (m), to the target and bolide properties in the strength regime, which is appropriate for this size range of impacts on Mars:

$$\frac{R}{a} = 0.725\left(\frac{\bar{Y}}{\rho v^2}\right)^{-0.20}\left(\frac{\rho_i}{\rho}\right)^{0.40} \text{ regolith} \quad \text{Eq. 7a}$$

$$\frac{R}{a} = 1.030\left(\frac{\bar{Y}}{\rho v^2}\right)^{-0.205}\left(\frac{\rho_i}{\rho}\right)^{0.40} \text{ cohesive sediments} \quad \text{Eq. 7b}$$

$$\frac{R}{a} = 0.930\left(\frac{\bar{Y}}{\rho v^2}\right)^{-0.275}\left(\frac{\rho_i}{\rho}\right)^{0.40} \text{ bedrock} \quad \text{Eq. 7c}$$

where a is the bolide radius (m), v the velocity (m/s), ρ_i the density (kg/m^3) of the bolide, $\bar{Y}$ the strength (Pa), and ρ the density (kg/m^3) of the target material. Numerical estimates of the

exponents are from Holsapple and Schmidt (1987). Target properties determine the final shape of the crater, and crater radius is a function of the cohesiveness, water content, and porosity of the target material. Eq. 7 allows us to determine the bolide radius, a, from which we can then derive the momentum of the impactor, assuming a spherical impactor of volume $4/3\pi a^3$, a chondritic bolide density of 3700 kg/m^3 for ρ_i (Williams et al., 2014), and impact velocities of either 6.5 or 11.5 km/s. These relationships predict craters of different diameters would be produced by bolides with equivalent starting momentum.

The entirety of craters in our studied dataset are simple craters, likely formed in loosely consolidated or sedimentary materials (Daubar et al., 2014a). However, we also considered the effects of bedrock materials, therefore we adopted three possible scenarios for scaling our observed crater radii into bolide momentum for the seismological modeling: regolith (Eq. 7a), cohesive sediments (Eq. 7b), and hard rock/bedrock (Eq. 7c); all values used in our calculations are presented in Table 1. Note that we do not scale for the effects of ejecta produced for different target materials.

Theoretical curves for these scaling relationships are shown in Fig. 3. For a 0.5 m radius crater and this distribution of target materials, bolide momentum ranges from 2.1×10^2 to 1.9×10^3 Ns, corresponding to values of impact source durations τ ranging from 0.14 to 0.19 s. Since we cannot directly constrain the size of the bolide, nor its initial velocity, we study a range of possible momentums and source durations. For a given target material there is only a 10–12% difference in momentum and a 2–5% difference in τ between impact velocities of 6.5 km/s and 11.5 km/s. Given this small difference, we adopt 6.5 km/s as our reference bolide velocity (Fig. 3), although it is likely smaller bolides that have fragmented during descent may be substantially decelerated by the atmosphere to lower velocities. Furthermore, we calculate the angle of momentum transfer with Eq. 5 using the observed impact angle and derived force impact angle where available from (Fig. 2). From these models, the momentum, seismic amplification factor, and source duration are used to generate synthetic seismograms and study the decay of amplitudes for seismic phases originating from our clustered impact sources.

4 Martian Background Model and Synthetic Seismograms of Impacts

For the 1-D background structure for our synthetic wave propagation simulations, we assume the velocity model EH45 of Rivoldini et al., (2011). We add a 100-m thick veneer of regolith, sediments, or bedrock to their model at the source depending on the proposed near surface materials for each impact (Table 1). This additional layer does not add significantly to the total travel times of teleseismic waves (adding ~ 30 milliseconds for the regolith case). EH45 was chosen as our reference, as this model incorporates martian geodesy constraints, geochemical constraints on the composition of the crust and mantle, and provides thermoelastic properties using equations of state (Rivoldini et al., 2011). Furthermore, it is a model used by the InSight team for pre-mission planning activities as it is judged to be the most likely scenario at Mars until models can be updated using seismic data (Clinton et al., 2017). The attenuation structure of the martian interior depends heavily on the amount of volatiles, heterogeneity, and thermal properties of the interior; in EH45 shear attenuation is assigned the Preliminary Reference Earth Model (PREM) values (Dziewonski & Anderson,

1981) for the crust (quality factor, Q=600) and the mantle (Q=143), with a bulk attenuation (Q=57822) throughout the mantle. The high secular acceleration of Phobos when translated to the seismic frequency range (Q=200) suggests PREM is appropriate for the martian mantle (Zharkov & Gudkova, 1997). Global waveforms for the martian model were then calculated using AxiSEM (Nissen-Meyer et al., 2014) and are comparable to those distributed via Instaseis (van Driel et al., 2015) for the EH45Tcold_1s model computed at 1 second (Ceylan et al., 2017). We use an explosive moment tensor with a radiation pattern that is unity in all directions, and then use the resulting seismograms to globally extrapolate the outcome to a local 3-D seismic source simulation (Fig. 4).

To determine the full wavefield response in the near vicinity of an impact cluster, we use an open-source 3-D finite-difference code, Serpentine Wave Propagation (WPP), (Petersson & Sjögreen, 2010) to model the impact source function (Eq. 6). WPP solves the equation of motion using 3-D finite difference, on a non-uniform Cartesian mesh, and is designed to run on parallel multi-CPU clusters. The code is primarily used for regional simulations of wave propagation in complex media. The elastic response of the medium is calculated for dominant frequencies up to 100 Hz or greater, though computational resources required grow for higher frequencies. To model clustered impacts with WPP, we added cluster impacts distributed in space and time and study the evolution of the seismic wavefield at frequencies up to 100 Hz within 10 km of the impact. Each 3-D simulation within WPP is specified on a 20 × 20 km surface area, up to 20 km depth, with an initial grid spacing of 20 meters at 20 km depth, and refined to 10 meters at 1 km depth, and 5 meters at 100 meters depth. The velocity and density of the upper 100 meters were modified to match the impact target properties given in Table 1 and calculated impact momentum and source durations. For each simulation, we calculated 20 seconds of seismograms and placed stations every 1 km from the source (Fig. 5). The resulting WPP seismograms had a sampling frequency of 2000 Hz, and approximately 20 points per wavelength, and allowed us to fully resolve a 10 Hz P-wave in the lowest velocity model (regolith).

The WPP simulations allowed us to study the near source response and detectability of an impact. Fig. 4b shows that the energy radiated from impacts should extend significantly into frequencies greater than 1 Hz, demonstrating that the detectability of impacts is an inherently high frequency, short period seismology endeavor (e.g., Teanby, 2015). However, extending the 3-D simulation to greater distances at high frequencies is computationally expensive for most modern wave propagation codes. Therefore, to study the detectability of impacts at greater distances, we couple our local 3-D synthetics to the 1-D global synthetics by scaling the power spectrum from the WPP synthetics to the epicentral decay and attenuation loss expected at higher frequencies. The epicentral decay loss is shown in (Fig. 4c), while the attenuation loss is obtained using a multiplication factor of $\exp(^{-\omega c}/_{2Qx})$, where Q=143, c =5.0 km/s, and ω is the angular frequency. Examples for this scaling across 3 impact sizes are shown in Fig. 6. Although this approach does not allow us to study the amplitude evolution of a particular seismic phase, it enables us to determine if the power spectral density of the impact source will fall above the detectable noise limit of the InSight seismometers.

Impact angle will affect the radiation pattern of energy emitted by an impact, so we used WPP and our source model to vary ψ_V and study the radiation pattern (Fig. 7). To recover the radiation pattern, we introduced receivers along the surface of a hemisphere below the impact at 5 km radius from the source location. The amplitude and polarity of the first motion was recorded, allowing us to map the variation in the source radiation pattern about the impact source. Note that because stations were located in the subsurface, the polarity reversal for P-waves expected at the free surface was not present in the subsurface stations. For vertical impacts ($\psi_V = 0°$), our simulations reproduced the explosive moment tensor frequently associated with an impact source in seismology (Aki & Richards, 2002). However, because our source is formulated as a directed transfer of momentum, as the impact becomes subvertical, there is a deviation from a simple explosive moment tensor, with the impact aquiring a directivity and polarity reversal in the impact azimuth ϕ_I. Furthermore, as the force becomes more horizontal, the energy is partitioned increasingly onto the horizontal components of motion, in this example case (0° azimuth), onto the North-South component of motion. For single station seismometers, detection of azimuthal variations in radiation pattern is not feasible owing to sampling only a single azimuth of the radiation pattern, although a future martian network may see such effects. This modeling further suggests that cluster impacts formed by impactors moving away from the seismometer are weakly radiating energy and are less detectable than impacts formed by impactors moving towards the seismometer.

To determine the detectable range of impacts, we used a noise floor and background noise estimate in combination with the expected amplitude decay from geometric spreading and attenuation effects modeled above. We adopted the measured noise floors (Mimoun et al., 2017) for the Seismic Experiment for Interior Structure (SEIS) short period (SP) and very-broad-band (VBB) instruments (Lognonné et al. 2019) (Fig. 6) and use the maximal radiation pattern of an impact to evaluate the distance that these instruments would be capable of detecting the ground impact of a bolide. For comparison, the noise floor of the Viking 2 seismometer (Anderson et al., 1976; Lorenz, 2012) at 1 Hz is ~60 dB above the SEIS noise floors, and the peak sensitivity of the Mars Science Laboratory (MSL) Inertial Measurement Units (IMU) on the Curiosity Rover is 10^{-4} $ms^{-2}Hz^{-1/2}$ at 3 Hz (10 mGal, or −80 dB of Fig. 6), or ~90 dB above the SEIS noise floors (Lewis et al., 2019). By examining the difference between the calculated spectra in Fig. 6 from the relevant instrumental noise floor, we establish the distance at which the impact is detectable by that instrument for a given signal to noise ratio (SNR); where each 10 dB change corresponds to a factor of 10 increase in the SNR of an event (Fig. 8). Higher noise environments tend to mask the signal, while low noise environments should allow us to approach the instrumental noise floor of SEIS (Mimoun et al., 2017). The result from this experiment shows that craters < 1 meter in diameter are detectable only in the very near field of the SEIS instruments (< 10 km), while the seismic signature of an impact producing a 100 m diameter crater would be detectable by SEIS at teleseismic distances > 3000 km (50.7°), the near field (< 100 km) on Viking, and not detected by the MSL IMUs. This agrees with previous results from Teanby and Wookey (2011), Teanby (2015), and Daubar et al. (2018).

Our results up to this point were calculated for singular impact events. In the next section we expanded our modeling to include the detectability of cluster impact craters forming

concurrently in a singular impact event. This next step combined the measured distribution of crater size, relative geographic position, and inferred impact angle and azimuth to predict the seismic signals of these events using the modeling tools described above.

5 Impact Cluster Synthetic Seismogram Modeling

Crater clusters are common on Mars and are likely to be far more visible in orbital images than individual impacts, making them a high science priority target for InSight (e.g., Daubar et al., 2018) and other future seismic missions. In particular, joint detection of a seismically recorded impact event and identification of the corresponding impact in images will provide a precise hypocenter and estimate of source size (crater diameter). This increases the value of an impact event for determining the internal structure of Mars.

Each cluster event in our impact crater database was parameterized by crater size, relative position, and inferred impact angle and direction. We assumed subsequent impact events proceed in the inferred direction of flight and we used the impact angle and assumed impact velocity to compute the horizontal distribution in time of source initiation times. Crater clusters have highly variable geographic dispersion, ranging from 6–721 meters. Dispersion of a cluster was defined here as the standard deviation of distances (in meters) between each possible combination of pairs of craters in the cluster and included in the database of (Daubar et al., 2019). For a 6.5 km/s bolide with an impact angle of 45° (typically expected value), the horizonal component of velocity is 4.5 km/s, resulting in origin time offsets on the order of 17–160 milliseconds. The time offsets are less for higher velocity bolides (9–90 milliseconds). Temporally resolving the seismic signals of individual impacts at teleseismic distances would be difficult using SEIS as the maximum sample rate of the instruments is 100 samples per second, or approximately 10 milliseconds of time resolution or 20 milliseconds at the Nyquist frequency (e.g., Panning et al., 2017). We have resampled and low pass filtered all synthetic results at 50 Hz to replicate this limitation in the InSight dataset. As with the previous section, each 3-D simulation within WPP is specified on a 20 × 20 km surface area, up to 20 km depth, with an initial grid spacing of 20 meters at 20 km depth, and refined to 10 meters at 1 km depth, and 5 meters at 100 meters depth (Fig. 9). For all of the cluster simulations, we assumed an impact velocity of 6.5 km/s and a target material consisting of 100 meters of cohesive sediments underlain by bedrock (Table 1). Note that none of our impacts in our database would penetrate into the deeper bedrock layer.

For the clusters in our database we calculated the expected amplitudes in the 20 × 20 km box finite difference grid and extrapolated to teleseismic distances incorporating the effects of geometric spreading and attenuation using the same methodology as outlined in Section 4. As in Section 4, we determined the detectable range of impacts clusters by using the difference between the calculated response power spectrums and the noise floors for the SEIS SP and VBB instruments (Fig. 8). The crater cluster is considered detectable by the SEIS instrument when it is above this noise floor (0 dB). This is repeated by placing a station every 5° in azimuth around the cluster to evaluate the effects of source radiation pattern. We reported an uncertainty in the cluster detection limit by finding the standard deviation across each azimuthal measurement and used it to capture the radiation pattern effects. Thus, higher uncertainties represented more variability in the source radiation

pattern as a function of backazimuth to the cluster location. We also selected the peak corner frequency from the acceleration spectrum to estimate the effects of combining impacts of different sizes and dependency on source duration (Eq. 2). The results of these analyses are plotted in Fig. 10, peak corner frequency, and Fig. 11, the distance of cluster detectability.

The peak corner frequency of the impact clusters consistently fell above the expected peak corner frequency for a similar sized single impact crater. Here we used the effective crater diameter (D_{eff}) to represent the size of the crater that would result if the individual impact craters in a cluster were formed by a single impact event (Daubar et al., 2019). This allowed us to compare the behavior of the clusters to a singular impact of similar effective size. In Fig. 10, an impact producing a crater 20 m in diameter was compared to several clusters of similar size. In all cases, the clusters produced a slightly more energetic source, and shifted the peak energy to higher frequencies. We observed that this is characteristic of nearly all of our impact clusters simulations (Fig. 10b,c), with the peak frequency of a cluster being increased by a factor of 1.5 to 2.0 times over the corresponding singular impact crater size. For the largest effective crater sizes this effect becomes muted; the larger craters propagate energy to greater epicentral distances and thus undergo more attenuation, especially at higher frequency. This erodes the higher frequency end of their power spectra and these clusters resembled the singular impacts of similar effective size at large epicentral distances.

We found that the detectability of impact clusters at small effective crater diameters is higher than for equivalent sized singular impacts (Fig. 11). As crater size increases, the clusters became similar to their individual impact counterparts, with detectability being controlled by lower frequencies of the power spectra as attenuation removed the energy from smaller impacts from the source. This was also observed in the peak corner frequency behavior in Fig. 10. There was causative relationship between the number of craters in a cluster and effective crater diameter, so as a rule, larger numbers of craters in a cluster enhances detectability (Fig. 11b). We did not observe any correlation between cluster geographic dispersion and detectability (Fig. 11c); the most dispersed clusters in our dataset represent populations of both endmembers of seismically detectable impacts. We observed a decrease in detectability as impact angles become more horizontal (Fig. 11d). This results from our scaling of the imparted momentum by the amount lost to ejecta in (Eqs. 4–5), which reduces the seismic efficiency and transfer of force into the target materials and partitioned energy between the horizontal and vertical components of motion and notably neglects the inherent asymmetry of ejecta momentum transfer. A similar reduction in amplitude is seen in the impact angle experiments presented in Fig. 7: as the incidence angle increases, the radiation patterns becomes significantly weaker for a fixed impact crater diameter.

6 Discussion

Based upon the positions of our 77 measured and dated impact sites on Mars and the location of the InSight seismometer in Elysium Planitia, no measured cluster in our database would have been detected by SEIS. Furthermore, none would have been detected by Viking 2 (assuming it was still operational), or the MSL IMUs (assuming they were turned on and recording). The closest cluster event to InSight in our database was located 840 km away (~14° epicentral distance on Mars), with over 90% of the clusters in the database situated at

distances of 4000 km (68°) or greater. For Viking 2, the closest cluster was 440 km away (7°), although this particular cluster would have been below the noise floor of the instrument at this distance. The closest cluster to MSL was 930 km away (16°), although this cluster was well below the noise floor of the IMUs at this distance as well. The estimate by (Teanby, 2015) for detectable events assumed the SEIS-SP noise floor, and they found that Mars would have a nominal detection rate of 1–3 impacts/year at distances < 1200 km (20°) although they also present a more optimistic scenario of up to 10–30 impacts/year given the uncertainties. Our modeling showed that the largest effective cluster in our database would have been detectable by the SP if it fell within a distance <1930 km (33°) from SEIS.

If we relaxed our requirement that the impact signal must fall above the SP noise floor and instead investigated the VBB noise floor, which is approximately 20 dB more sensitive than the SP instrument, we found that two of the crater clusters fall just above the instrument self-noise. If we instead used SEIS-VBB, the first detectable event is a cluster of 66 craters with an effective diameter of 21.6 m at a distance of 4860 km (82°), and the second being our largest impact crater cluster, with 285 craters, and an effective diameter of 33.8 m, at a distance of 2780 km (47°). These events would sample the deep martian interior and would have been valuable science targets for the mission if recorded by InSight. This estimate did not take into account the environmental noise around InSight and the noise that could obscure signals close to the instrument noise. However, martian background noise is estimated to be near the noise floor of the VBB at the landing site (Banerdt et al., 2019; Mimoun et al., 2017).

Translating these detections into a rate of detections would require temporal constraints on how many clusters are produced per year, and our impact crater database is incomplete. For tractability, only 77 clusters were selected for analysis out of ~300 known new dated clusters. Additionally, the larger set of known small and recent impact events is biased towards dusty regions where disturbance of high albedo surface dust increases their visibility from orbit (Daubar et al., 2013; Malin et al., 2006). InSight will provide a chance to fill in these gaps and listen for impact events that would otherwise be unnoticed in repeat images.

Impact cluster detectability is also affected by our assumptions of material properties and choice of model for scaling the effects of ejecta. We have assumed that ejecta are produced for a lunar-like target, and more cohesive materials on Mars may increase the ejecta amplification effects. We also assumed symmetry in the ejecta partitioning of momentum in the impact, breaking this symmetry would enhance the horizontal component of the force in our simulations and alter the patterns seen in Fig. 7, making our estimates an upper bound on the effect of impact angle on detectability. The choice of target material and scaling law for impact momentum affect the detectability by changing the relative size of the source for a given known crater size. For a fixed bolide momentum, we observe a one order magnitude change in the size of the resultant impact crater going from regolith to hard bedrock in the scaling law of Eq. 7. However, this large change in seismic efficiency is offset by waveform effects in these layers, which are visible in Fig. 5; the low velocity regolith generates a reverberation sequence that initially amplifies the waves, a feature demonstrated in the waveform modeling presented in (Daubar et al., 2018). This effect is absent in the more consolidated target materials and disassociates the amplitudes between the different target

material properties. Furthermore, the internal attenuation of Mars is unknown and scattering of energy similar to the Moon may exist. Here we assume the model of (Rivoldini et al., 2011), which places values similar to the Earth's upper mantle throughout the mantle and crust. If attenuation is lower (or higher), impact detectability would improve (or degrade). Currently, our best constraint comes from examination of the secular acceleration of Phobos, which suggests Q=200, similar to the upper mantle of Earth, in the seismic band for the martian mantle (Zharkov & Gudkova, 1997). Fortunately, any scaling of the local impact source to teleseismic distances can be refined once InSight provides a more detailed constraint on the attenuation structure of Mars.

Impact clusters are likely the result of the breakup and disintegration of a bolide(s) in the martian atmosphere. In particular, bolides that breakup in the atmosphere may slow down considerably and change the impact velocity at the surface. This would require larger bolide masses to produce the same sized impact crater, since we examine the momentum associated with a particular crater size, there is a direct trade between bolide velocity and mass. Atmospheric signals from bolides striking the Earth are distinct and observed on global networks of acoustically sensitive infrasound instruments, as well as seismometers (Hedlin et al., 2018; Wei et al., 2018). It is expected that InSight will detect similar signals, and there are multiple approaches that have been presented to characterize the acoustic signature of bolide breakup in the atmosphere (Collins et al., 2017; Daubar et al., 2018; Ivanov et al., 2009; Karakostas et al., 2018; Popova et al., 2007; Stevanovic et al., 2017; Williams et al., 2014). Although we only address the ground transmitted signals here, it is possible that a non-detected event on the ground may still be recorded in the atmosphere. If InSight is fortunate to record both, the joint detection will be an unprecedented opportunity to observe the impact process in a relatively quiet environment free of the cultural and atmospheric noise of Earth.

From an observational perspective, an impact cluster will spectrally resemble a nearby smaller crater. The clusters exhibit a shift in the peak frequency to higher frequency and power, which emulates the effects of a nearby smaller and singular impact. The assumption that the crater size can be estimated from the peak spectral frequency thus needs to be caveated with the exception that a higher peak frequency could also indicate a more distant cluster. For larger and more distant clusters, this effect is lost, but would still be relevant when a large impact occurs near InSight and a spectral excess of energy is observed in the frequency range of 1–5 Hz. There is also a decrease in power associated with lower frequencies for the impact source (Fig. 4). This characteristic would be useful for distinguishing between tectonic and impact events, as discussed in (Daubar et al., 2018). Furthermore, with only a single seismometer it is difficult to study the source radiation pattern of any recorded impacts, but the models here suggest that measurement of the azimuthal variation and polarization of energy onto horizontal and vertical components should reveal information about the orientation of the path of the incoming bolide, including azimuth, and impact angle. Future missions incorporating a network of instruments would be able to use this technique to make an important step in impact monitoring and studies of the impact process.

7 Summary and Conclusions

We investigated the seismic signatures of recently formed impact craters on Mars using a momentum transfer model that translates crater size into the expected seismic source function. The model is used to determine the contribution of target material properties, bolide trajectory, and crater size into estimates for the source radiation pattern and detectability of both singular impacts and clusters of closely associated impact craters. The detectability of the resulting source is investigated as a function of the azimuth and distance from the impact or impact cluster and used to derive an estimate for the observable distance and frequency of the impact on the InSight SEIS seismometers.

These experiments reveal that impact clusters have seismic properties that can be used to distinguish them from singular impact events. The peak corner frequency of impact clusters is moved to higher frequencies as a result of energy contributed by smaller craters to the overall power spectrum. The clusters are detectable at greater epicentral distances than singular impacts due to the additional power added by combining multiple sources together. Our experiments also show that at great epicentral distances, the signature of the impact cluster is dominated by the largest crater in the cluster and resembles that of a single large impact. We also find that the time separation between individual impacts in a cluster is small and individual impact events cannot be resolved unless the instrument is situated < 10 km from the impacts.

Based upon these simulations, only two of the clusters in our database (D_{eff} > 20 m) would be detectable by the InSight VBB instrument, with the assumptions that the martian background noise is low, and attenuation is also low. None of these events would have been detected by the Viking 2 or MSL IMU instruments, although we did not analyze the entirety of the larger database of fresh and recent impact craters. The uncertainties in these parameters is high and will require details about the martian noise environment and background seismic structure to be refined. In the scenario where there is a detection of an impact by SEIS and a subsequently obtained image of the newly formed crater(s), the resulting precise source location will have similar scientific value to the impacts of the Apollo SIVB and Lunar Modules on the surface of the Moon. In addition to constraints on the internal structure of Mars, joint seismic and image derived source locations will enable for the testing of many of these models and their underlying assumptions against the impact process on Mars.

Acknowledgements

This research was supported by grants NASA-MFRP NNX14AQ92G (NS, ID, and MB) and NASA InSight Participating Scientist 80NSSC18K1628 (NS). We thank the Editor, Associate Editor Gareth Collins, Taichi Kawamura, and an anonymous reviewer for their suggestions and comments that greatly improved the clarity and quality of the manuscript. The figures in this manuscript were generated using the Generic Mapping Tools (Wessel & Smith, 1998). Data analysis made use of the Seismic Analysis Code (Goldstein, 2003), and Serpentine Wave Propagation Program (Petersson & Sjögreen, 2010). A portion of this research was carried out at the Jet Propulsion Laboratory, California Institute of Technology, under a contract with the National Aeronautics and Space Administration. The impact crater database used in producing this manuscript are presented in the online supplement of (Daubar et al., 2019) and synthetic waveforms are archived at https://doi.org/10.13016/asq5-ugzd. This is paper is InSight Contribution Number 46.

References

Aki K, & Richards P (2002). Quantitative Seismology (2nd ed.). Sausalito: University Science Books.

Anderson DL, Duennebier FK, Latham GV, Toksoz MF, Kovach RL, Knight TCD, et al. (1976). Viking Seismic Experiment. Science, 194(4271), 1318–1321. doi:10.1126/science.194.4271.1318 [PubMed: 17797092]

Anderson JLB, Schultz PH, & Heineck JT (2004). Experimental ejection angles for oblique impacts: Implications for the subsurface flow-field. Meteoritics & Planetary Science, 39(2), 303–320.

Banerdt WB, Smrekar S, Antonangeli D, Asmar S, Banfield D, Beghein C, et al. (2019). Insight-The First Three Months on Mars. Paper presented at the Lunar and Planetary Science Conference.

Banerdt WB, Smrekar S, Hoffman T, Spath S, Lognonné P, Spohn T, et al. (2017). The InSight Mission for 2018. Paper presented at the 48th Lunar and Planetary Science Conference, The Woodlands, Texas.

Ceylan S, van Driel M, Euchner F, Khan A, Clinton J, Krischer L, et al. (2017). From Initial Models of Seismicity, Structure and Noise to Synthetic Seismograms for Mars. Space Science Reviews, 211(1–4), 595–610. doi:10.1007/s11214-017-0380-6

Cheng AF, Michel R, Jutzi M, Rivkin AS, Stickle A, Barnouin O, et al. (2016). Asteroid Impact & Deflection Assessment mission: Kinetic impactor. Planetary and Space Science, 121, 27–35.

Clinton JF, Giardini D, Lognonne P, Banerdt B, van Driel M, Drilleau M, et al. (2017). Preparing for InSight: An Invitation to Participate in a Blind Test for Martian Seismicity. Seismological Research Letters, 88(5), 1290–1302. doi:10.1785/0220170094

Collins GS, Lynch E, McAdam R, & Davison TM (2017). A numerical assessment of simple airblast models of impact airbursts. Meteoritics & Planetary Science, 52(8), 1542–1560. doi:10.1111/maps.12873

Daubar I, Lognonne P, Teanby NA, Miljkovic K, Stevanovic J, Vaubaillon J, et al. (2018). Impact-Seismic Investigations of the InSight Mission. Space Science Reviews, 214(8). doi:10.1007/s11214-018-0562-x

Daubar IJ, Atwood-Stone C, Byrne S, McEwen AS, & Russell PS (2014a). The morphology of small fresh craters on Mars and the Moon. Journal of Geophysical Research-Planets, 119(12), 2620–2639. doi:10.1002/2014JE004671

Daubar IJ, Banks ME, Schmerr NC, & Golombek MP (2019). Recently Formed Crater Clusters on Mars. Journal of Geophysical Research: Planets, 0(0). doi:10.1029/2018je005857

Daubar IJ, Dundas CM, Byrne S, Geissler P, Bart GD, McEwen AS, et al. (2016). Changes in blast zone albedo patterns around new martian impact craters. Icarus, 267, 86–105. doi:10.1016/j.icarus.2015.11.032

Daubar IJ, McEwen AS, Byrne S, Kennedy MR, & Ivanov B (2013). The current martian cratering rate. Icarus, 225(1), 506–516. doi:10.1016/j.icarus.2013.04.009

Daubar IJ, McEwen AS, Byrne S, Kreslavsky M, Saper L, & Kennedy MR (2014b). New Dated Impacts on Mars and the Current Cratering Rate. Meteoritics & Planetary Science, 49, A90–A90.

Davis PM (1993). Meteoroid Impacts As Seismic Sources On Mars. Icarus, 105(2), 469–478. doi:10.1006/icar.1993.1142

Dziewonski AM, & Anderson DL (1981). Preliminary Reference Earth Model. Physics of the Earth and Planetary Interiors, 25(4), 297–356. doi:10.1016/0031-9201(81)90046-7

Edwards WN, Eaton DW, & Brown PG (2008). Seismic Observations of Meteors: Coupling Theory and Observations. Reviews of Geophysics, 46(4).

Goldstein P, Dodge D, Firpo M, Minner L (2003). SAC2000: Signal processing and analysis tools for seismologists and engineers In Lee W, Kanamori H, Jenning P, Kisslinger C (Ed.), The IASPEI International Handbook of Earthquake and Engineering Seismology. London: Academic Press.

Golombek M, Warner NH, Grant J, Hauber E, Ansan V, Weitz C, et al. (2019). Geology of the InSight Landing Site, Mars: Initial Observations. Paper presented at the 50th Lunar and Planetary Science Conference, The Woodlands, Texas.

Gudkova T, Lognonne P, Miljkovic K, & Gagnepain-Beyneix J (2015). Impact cutoff frequency - momentum scaling law inverted from Apollo seismic data. Earth and Planetary Science Letters, 427, 57–65. doi:10.1016/j.epsl.2015.06.037

Gudkova TV, Lognonne P, & Gagnepain-Beyneix J (2011). Large impacts detected by the Apollo seismometers: Impactor mass and source cutoff frequency estimations. Icarus, 211(2), 1049–1065. doi:10.1016/j.icarus.2010.10.028

Gudkova TV, Lognonne P, Zharkov VN, & Raevsky SN (2014). On the scientific aims of the MISS seismic experiment. Solar System Research, 48(1), 11–21. doi:10.1134/S0038094614010043

Güldemeister N, & Wünnemann K (2017). Quantitative analysis of impact-induced seismic signals by numerical modeling. Icarus, 296, 15–27.

Harrington J, Lebeau RP, Backes KA, & Dowling TE (1994). Dynamic Response of Jupiter's Atmosphere to the Impact of Comet Shoemaker-Levy 9. Nature, 368(6471), 525–527. doi: 10.1038/368525a0

Hedlin MAH, Ritsema J, de Groot-Hedlin CD, & Hetland EA (2018). A Multidisciplinary Study of the 17 January 2018 Bolide Terminal Burst over Southeast Michigan. Seismological Research Letters, 89(6), 2183–2192. doi:10.1785/0220180157

Holsapple K, Giblin I, Housen K, Nakamura A, & Ryan E (2002). Asteroid Impacts: Laboratory Experiments and Scaling Laws In Bottke WF, Cellino A, Paolicchi P, & Binzel RP (Eds.), Asteroids III (pp. 443–462). Tucson: University of Arizona Press.

Holsapple KA (1993). The Scaling of Impact Processes in Planetary Sciences. Annual Review of Earth and Planetary Sciences, 21, 333–373.

Holsapple KA, & Housen KR (2007). A crater and its ejecta: An interpretation of Deep Impact. Icarus, 187(1), 345–356. doi:10.1016/j.icarus.2006.08.029

Holsapple KA, & Housen KR (2012). Momentum transfer in asteroid impacts. I. Theory and scaling. Icarus, 221(2), 875–887. doi:10.1016/j.icarus.2012.09.022

Holsapple KA, & Schmidt RM (1987). Point-Source Solutions and Coupling Parameters in Cratering Mechanics. Journal of Geophysical Research-Solid Earth and Planets, 92(B7), 6350–6376. doi:DOI 10.1029/JB092iB07p06350

Ivanov B, Melosh HJ, McEwen A, & Team TH (2009). Small Impact Crater Clusters In High Resolution Hirise Images - II. Paper presented at the LPSC XL, Woodlands, TX.

Ivanov BA, & Artemieva NA (2002). Numerical modeling of the formation of large impact craters In Koeberl C & MacLeod KG (Eds.), Catastrophic Events and Mass Extinctions: Impacts and Beyond (Vol. 356, pp. 619–630). Boulder: Geological Soc Amer Inc.

JeongAhn Y, & Malhotra R (2015). The current impact flux on Mars and its seasonal variation. Icarus, 262, 140–153. doi:10.1016/j.icarus.2015.08.032

Karakostas F, Rakoto V, Lognonne P, Larmat C, Daubar I, & Miljkovic K (2018). Inversion of Meteor Rayleigh Waves on Earth and Modeling of Air Coupled Rayleigh Waves on Mars. Space Science Reviews, 214(8). doi:UNSP 127 10.1007/s11214-018-0566-6

Lammlein DR, Latham GV, Dorman J, Nakamura Y, & Ewing M (1974). Lunar Seismicity, Structure, and Tectonics. Reviews of Geophysics, 12(1), 1–21.

Latham G, Ewing M, Dorman J, Press F, Toksoz N, Sutton G, et al. (1970a). Seismic Data From Man-Made Impacts On Moon. Science, 170(3958), 620-&. doi:10.1126/science.170.3958.620 [PubMed: 17799298]

Latham GV, McDonald WG, & Moore HJ (1970b). Missile Impacts As Sources Of Seismic Energy On Moon. Science, 168(3928), 242-&. [PubMed: 17747098]

Lewis KW, Peters S, Gonter K, Morrison S, Schmerr N, Vasavada AR, & Gabriel T (2019). A surface gravity traverse on Mars indicates low bedrock density at Gale crater. Science, 363(6426), 535-+. [PubMed: 30705193]

Lognonne P, Le Feuvre M, Johnson CL, & Weber RC (2009). Moon meteoritic seismic hum: Steady state prediction. Journal of Geophysical Research-Planets, 114 10.1029/2008je003294

Lorenz RD (2012). Planetary seismology-Expectations for lander and wind noise with application to Venus. Planetary and Space Science, 62(1), 86–96. doi:10.1016/j.pss.2011.12.010

Malin MC, Edgett KS, Posiolova LV, McColley SM, & Dobrea EZN (2006). Present-day impact cratering rate and contemporary gully activity on Mars. Science, 314(5805), 1573–1577. doi: 10.1126/science.1135156 [PubMed: 17158321]

McEwen AS, Eliason EM, Bergstrom JW, Bridges NT, Hansen CJ, Delamere WA, et al. (2007). Mars Reconnaissance Orbiter's High Resolution Imaging Science Experiment (HiRISE). Journal of Geophysical Research-Planets, 112(E5). 10.1029/2005je002605

McGarr A, Latham GV, & Gault DE (1969). Meteoroid Impacts As Sources Of Seismicity On Moon. Journal of Geophysical Research, 74(25), 5981–&. doi:10.1029/JB074i025p05981

Melosh J (1989). Impact Cratering: A Geologic Process: Oxford University Press.

Mimoun D, Murdoch N, Lognonne P, Hurst K, Pike WT, Hurley J, et al. (2017). The Noise Model of the SEIS Seismometer of the InSight Mission to Mars. Space Science Reviews, 211(1–4), 383–428. doi:10.1007/s11214-017-0409-x

Nakamura Y, Dorman J, Duennebi F, Ewing M, Lammlein D, & Latham G (1974). High-Frequency Teleseismic Signals From Shallow Lunar Sources. Transactions-American Geophysical Union, 55(4), 328–328.

Nakamura Y, Latham GV, & Dorman HJ (1982). Apollo Lunar Seismic Experiment - Final Summary. Journal of Geophysical Research, 87, A117–A123.

Nissen-Meyer T, van Driel M, Stahler SC, Hosseini K, Hempel S, Auer L, et al. (2014). AxiSEM: broadband 3-D seismic wavefields in axisymmetric media. Solid Earth, 5(1), 425–445. doi: 10.5194/se-5-425-2014

Ortiz JL, Aceituno FJ, Quesada JA, Aceituno J, Fernandez M, Santos-Sanz P, et al. (2006). Detection of sporadic impact flashes on the Moon: Implications for the luminous efficiency of hypervelocity impacts and derived terrestrial impact rates. Icarus, 184(2), 319–326. doi:10.1016/j.icarus.2006.05.002

Panning MP, Lognonne P, Banerdt WB, Garcia R, Golombek M, Kedar S, et al. (2017). Planned Products of the Mars Structure Service for the InSight Mission to Mars. Space Science Reviews, 211(1–4), 611–650. doi:10.1007/s11214-016-0317-5

Patton HJ, & Walter WR (1993). Regional Moment - Magnitude Relations For Earthquakes And Explosions. Geophysical Research Letters, 20(4), 277–280. doi:10.1029/93gl00298

Petersson NA, & Sjögreen B (2010). Reference guide to WPP version 2.0. Lawrence Livermore National Laboratory Technical Report, LLNL-TR-422928.

Plescia JB, Robinson MS, Wagner R, & Baldridge R (2016). Ranger and Apollo S-IVB spacecraft impact craters. Planetary and Space Science, 124, 15–35.

Popova O, Nemtchinov I, & Hartmann WK (2003). Bolides in the present and past martian atmosphere and effects on cratering processes. Meteoritics & Planetary Science, 38(6), 905–925.

Popova OP, Hartmann WK, Ivan VN, Richardson DC, & Berman DC (2007). Crater clusters on Mars: Shedding light on martian ejecta launch conditions. Icarus, 190(1), 50–73. doi:10.1016/j.icarus.2007.02.022

Richardson JE, Melosh HJ, Artemeiva NA, & Pierazzo E (2005). Impact cratering theory and modeling for the Deep Impact mission: From mission planning to data analysis. Space Science Reviews, 117(1–2), 241–267. doi:10.1007/s11214-005-3393-5

Rivoldini A, Van Hoolst T, Verhoeven O, Mocquet A, & Dehant V (2011). Geodesy constraints on the interior structure and composition of Mars. Icarus, 213(2), 451–472. doi:10.1016/j.icarus.2011.03.024

Shoemaker EM (1961). Interpretation of lunar craters In Kopal Z (Ed.), Physics and Astronomy of the Moon (pp. 283–359). London, UK: Academic Press Inc.

Speyerer EJ, Povilaitis RZ, Robinson MS, Thomas PC, & Wagner RV (2016). Quantifying crater production and regolith overturn on the Moon with temporal imaging. Nature, 538(7624), 215–218. doi:10.1038/nature19829 [PubMed: 27734864]

Stevanovic J, Teanby NA, Wookey J, Selby N, Daubar IJ, Vaubaillon J, & Garcia R (2017). Bolide Airbursts as a Seismic Source for the 2018 Mars InSight Mission. Space Science Reviews, 211(1–4), 525–545. doi:10.1007/s11214-016-0327-3

Teanby NA (2015). Predicted detection rates of regional-scale meteorite impacts on Mars with the InSight short-period seismometer. Icarus, 256, 49–62. doi:10.1016/j.icarus.2015.04.012

Teanby NA, & Wookey J (2011). Seismic detection of meteorite impacts on Mars. Physics of the Earth and Planetary Interiors, 186(1–2), 70–80. doi:10.1016/j.pepi.2011.03.004

Toksoz MN (1974). Geophysical Data and Interior of Moon. Annual Review of Earth and Planetary Sciences, 2, 151–177.

van Driel M, Krischer L, Stahler SC, Hosseini K, & Nissen-Meyer T (2015). Instaseis: instant global seismograms based on a broadband waveform database. Solid Earth, 6(2), 701–717. doi:10.5194/se-6-701-2015

Vasavada AR, Grotzinger JP, Arvidson RE, Calef FJ, Crisp JA, Gupta S, et al. (2014). Overview of the Mars Science Laboratory mission: Bradbury Landing to Yellowknife Bay and beyond. Journal of Geophysical Research-Planets, 119(6), 1134–1161. doi:10.1002/2014je004622

Walker JD (2003). Loading sources for seismological investigations of asteroids and comets. International Journal of Impact Engineering, 29(1–10), 757–769. doi:10.1016/j.ijimpeng.2003.10.022

Wei Z, Zhao LF, Xie XB, Hao JL, & Yao ZX (2018). Seismic characteristics of the 15 February 2013 bolide explosion in Chelyabinsk, Russia. Earth and Planetary Physics, 2(5), 420–429. doi:10.26464/epp2018039

Wessel P, & Smith WHF (1998). New, improved version of Generic Mapping Tools released. EOS Trans AGU, 79(47), 579.

Whitaker E (1972). Artificial Lunar Impact Craters: Four New Identifications In NASA Special Publication (Vol. 315, pp. 29–39): NASA Special Publication.

Williams JP, Pathare AV, & Aharonson O (2014). The production of small primary craters on Mars and the Moon. Icarus, 235, 23–36. doi:10.1016/j.icarus.2014.03.011

Zharkov VN, & Gudkova TV (1997). On the dissipative factor of the Martian interiors. Planetary and Space Science, 45(4), 401–407. doi:10.1016/s0032-0633(96)00144-4

Key Points:

- We model the seismic signature of single and cluster impact sources, approximating the impact(s) as a momentum transfer and directed force
- The seismic source of non-vertical impacts deviates from an explosive point source moment tensor, with amplitudes varying by azimuth
- Cluster impacts are distinguishable by a wider frequency spectrum and enhanced distance detectability over single impacts

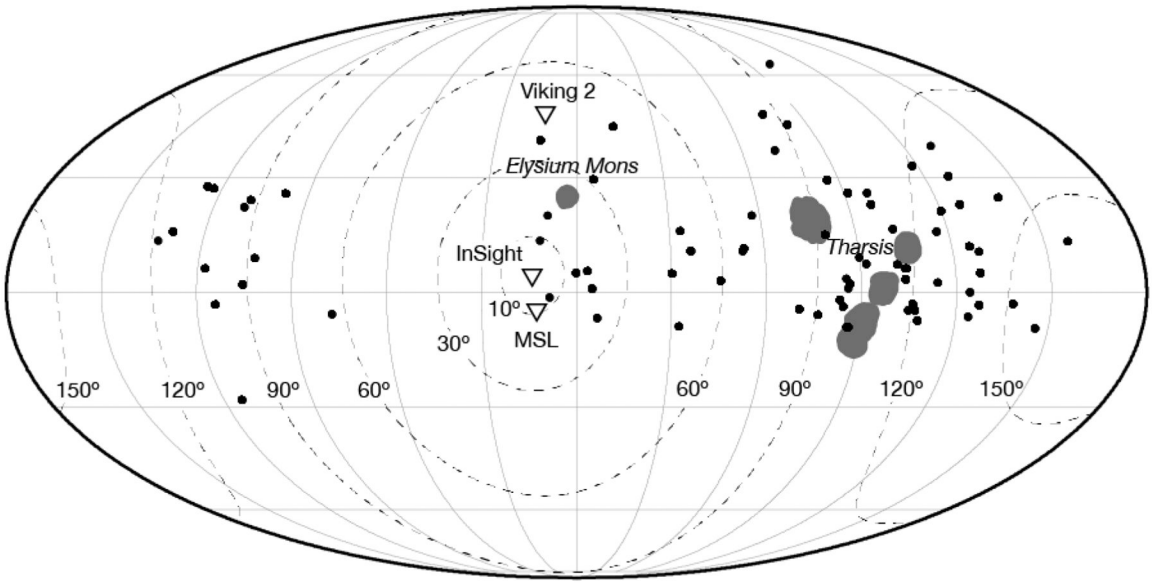

Figure 1.

The spatial distribution of our newly dated impact sites on Mars relative to the location of martian seismometers (triangles). The locations of craters and crater clusters are indicated with black circles. The landing site for the InSight mission (4.502°N, 135.623°E) (Golombek et al., 2019), locations of the Mars Curiosity Rover (4.5895°S, 137.4417°E) (Vasavada et al., 2014), and Viking 2 lander (47.6673°N, 134.2809°E; location from HiRISE image PSP_001501_2280) are indicated by inverted triangles. Major topographic volcanoes are indicated in dark gray. Broken lines indicate the epicentral distance from the InSight landing site. Map is a Mollweide projection centered on 150°E longitude, with gridlines spaced every 30° in latitude and longitude.

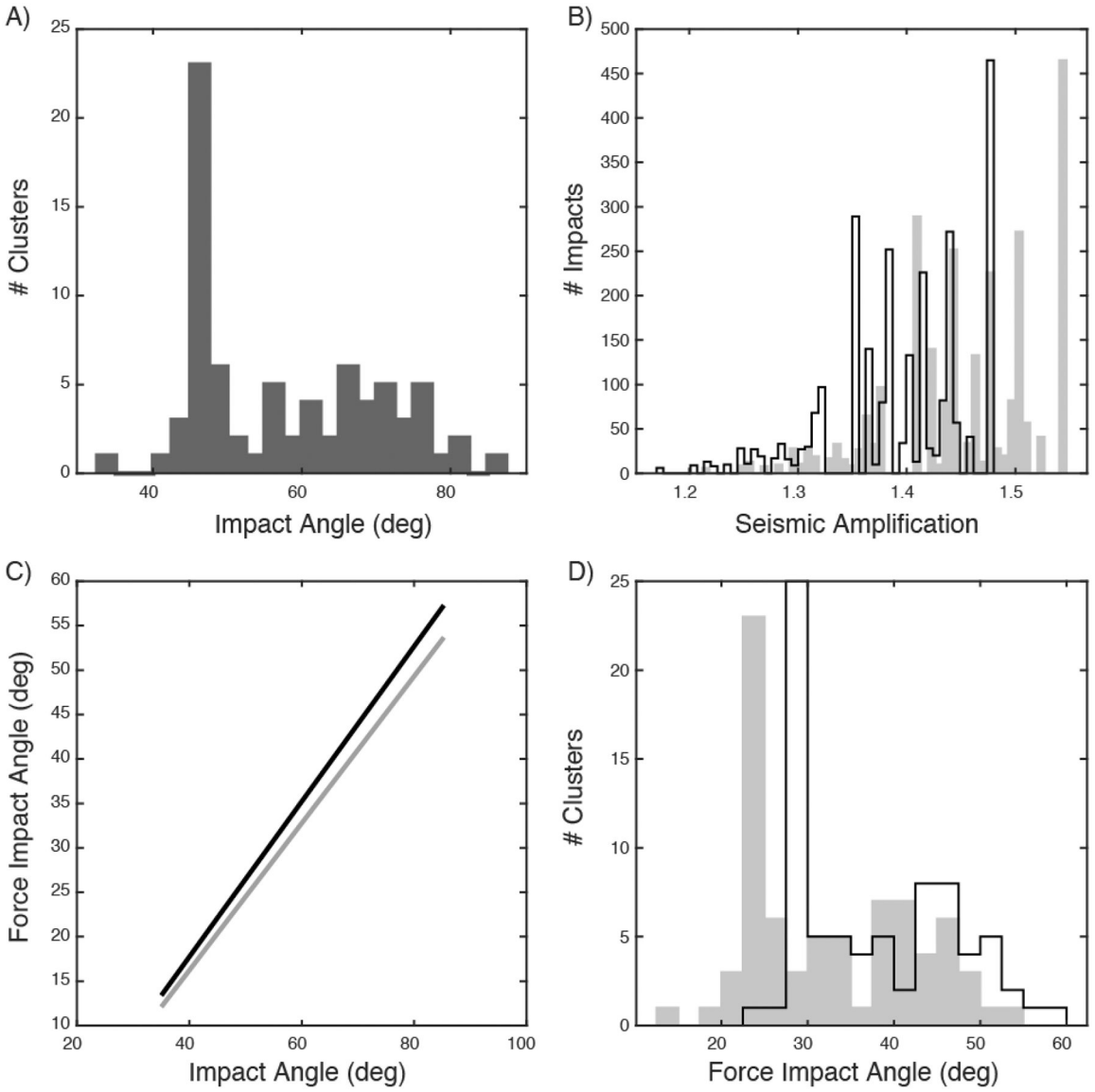

Figure 2.

Impact force angles and seismic amplifications derived for our database of impact clusters and individual craters (See Supplemental Table 2 in Daubar et al., 2019). A) Histogram of the measured impact angle, ψ_v from the clusters; this measurement is described in Section 3 and in more detail in (Daubar et al., 2019). Impact angle is measured from the vertical at 0°. The large peak at 45° is for clusters where we could not measure impact angle and assigned this value. B) Histogram of seismic amplification, S, derived from Eq. 4 and the impact angle in the (Daubar et al., 2019) database of individual craters; values are for bolide velocities of 6.5 km/s (solid line) and 11.5 km/s (light gray shading). There is a 4.3% difference between the mean S for 6.5 km/s (1.39) and 11.5 km/s (1.45) C) Relationship of the seismic force impact angle ψ_I to the impact angle from Eq. 5; values for bolide velocities are the same as in (B). D) Histogram of the force impact angles used to calculate the seismic response of the (Daubar et al., 2019) crater database; values for bolide velocities are the

same as in (B). The average force impact angle for 6.5 km/s is 34°, and for 11.5 km/s it is 33°; higher velocity shifts the force impact angle by 4.6% towards the vertical. All data used to create this figure are available in Supplemental Table 1.

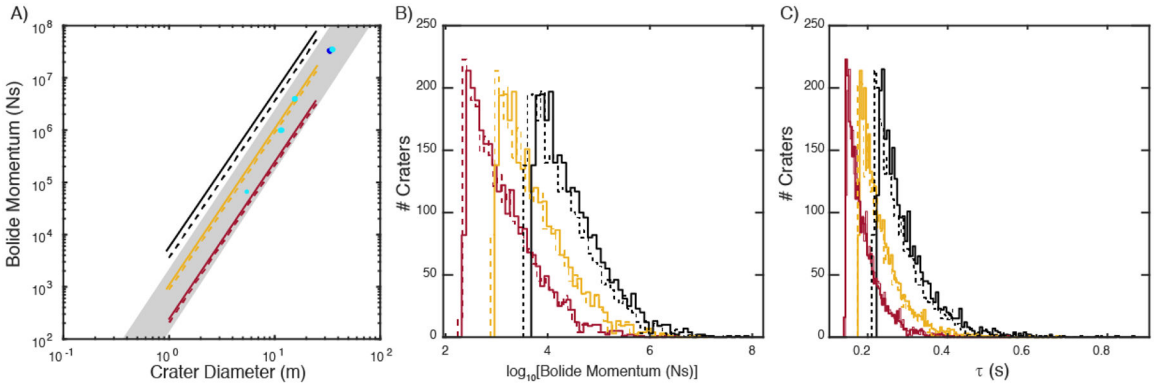

Figure 3.

Scaling law relationship between crater radius and the momentum imparted into the target for exciting seismic energy during an impact. A) Comparison of the results for the Eq. 7 scaling law for 6.5 km/s (solid line) and 11.5 km/s (broken lines) for bolide velocity. Material types are regolith (red), cohesive sediments (yellow), and bedrock (black). Crater diameters are derived from Supplemental Table 1 in (Daubar et al., 2019). Gray shading indicates range of scaling used by (Teanby & Wookey, 2011) for Mars, and circles are from lunar impact craters (Whitaker, 1972), cyan, corrected for martian gravity, and (Plescia et al., 2016), blue. B) Histograms of the bolide momentum obtained from using martian impact velocities (6.5, 11.5 km/s) and relevant material properties (see text) for Eq. 7, and the individual diameters measured in the (Daubar et al., 2019)crater database. Colors are the same as in part A. C) Histogram of source duration τ obtained using Eq. 2 to scale impact momentums of individual craters in our database. Colors are the same as in part A. All data used to create this figure are available Supplemental Table 1.

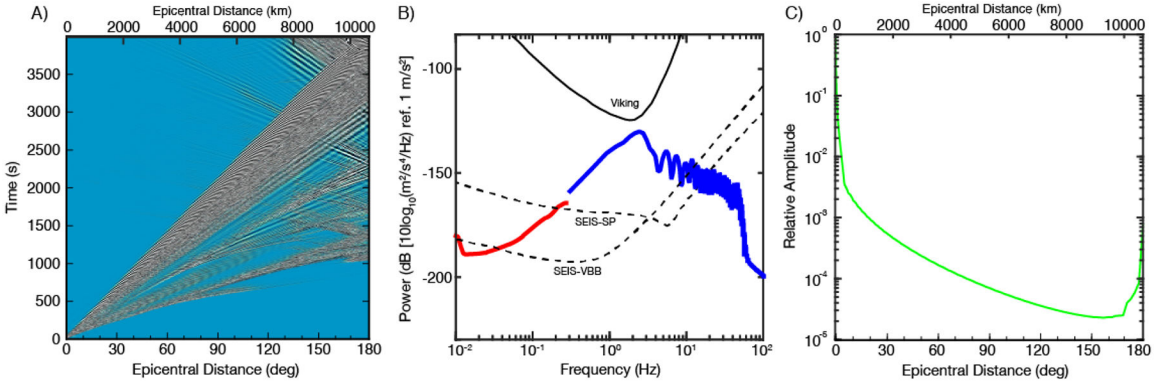

Figure 4.

Global synthetic vertical component seismograms calculated for the EH45 model (Ceylan et al., 2017) for a single 10-meter diameter crater. A) Epicentral distance moveout plot for acceleration waveforms generated from the global model. Amplitudes are normalized to the maximum amplitude at each distance, with the largest amplitudes typically surface wave arrivals. Synthetics are valid to ~0.4 Hz and generated using Instaseis (van Driel et al., 2015). B) Power density spectrum for the impact source, results from AxiSEM (red) are compared to the local simulation in WPP (blue), WPP results are available in the online supplement to this paper. Local source parameters specify a 6.5 km/s bolide hitting a cohesive sediment target at an angle of 45°. The directional force in the simulation is $2.1*10^6$ N with an impact corner frequency of 2.1 Hz. Power density spectra are calculated in Matlab using a Welch overlapping segment with 50% overlap, and each segment is windowed with a Hamming window. The Viking 2 seismometer noise floor (solid black) (Anderson et al., 1976; Lorenz, 2012), along with the Seismic Experiment for Interior Structure (SEIS)-VBB and SEIS-SP noise floors (broken lines) (Mimoun et al., 2017) are also indicated. Seismograms are low-pass filtered at 0.2 Hz for the 1-D simulation, and 50 Hz for the 3-D simulation. C) Amplitude decay across epicentral distance for the global model shown in (A). Peak amplitude is measured in the spectral domain and normalized to the maximum at 0 km epicentral distance.

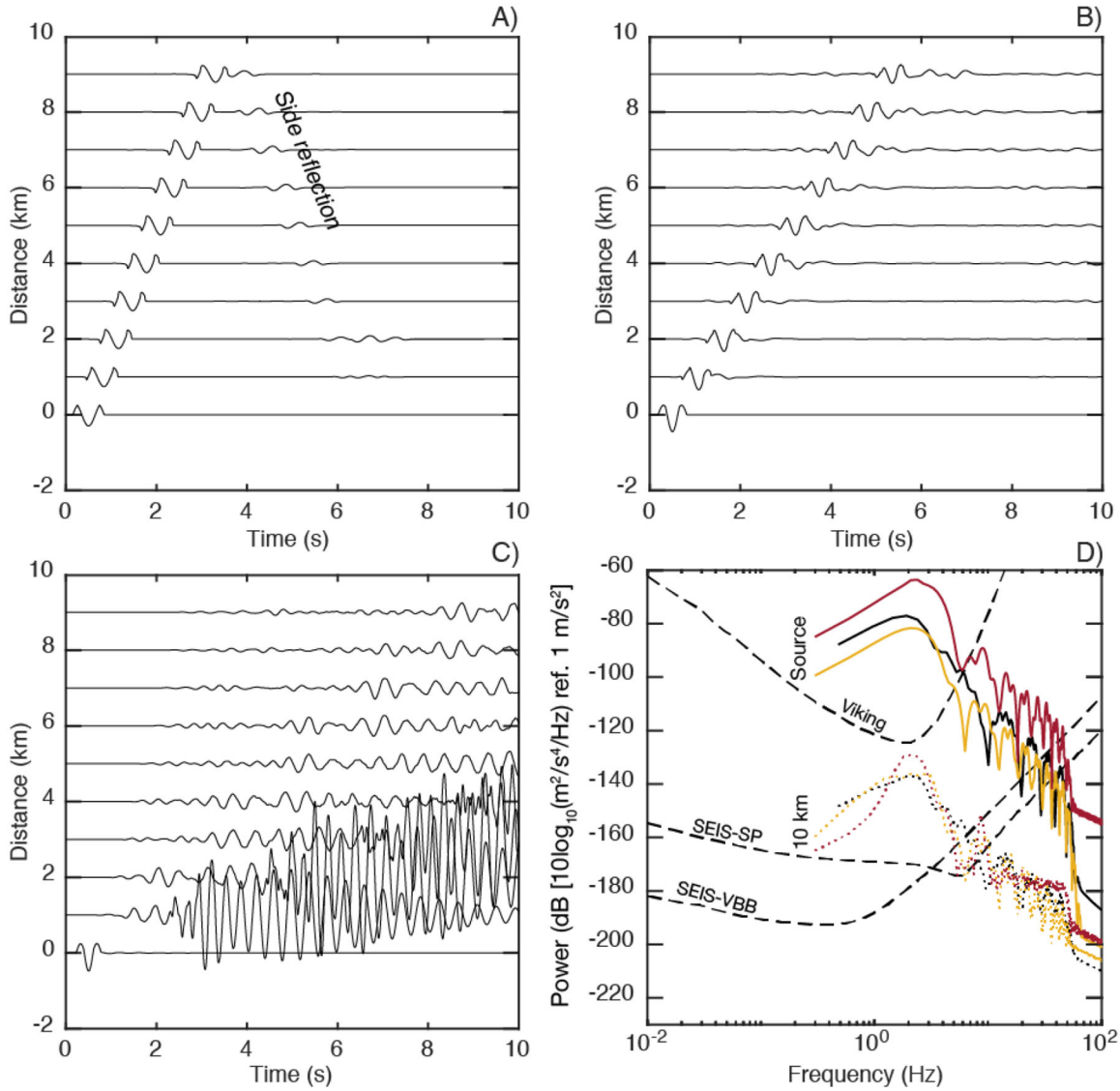

Figure 5.

Synthetic seismograms generated for an impact source into various target materials, each producing a 10 m diameter crater at an impact angle of 45°. The simulation was generated for the same impact source shown in Fig. 4, except the uppermost portion of the model had a different target type (Table 1). In panels A-C, seismograms are normalized by the peak amplitude at each distance in the 0–6 second window. A) Waveforms for a bedrock target; specified impact force is $8.7*10^6$ N. A side reflection from the WPP simulation is labeled in the panel. B) Waveforms for a cohesive sediment target; specified impact force is $2.1*10^6$ N. C) Waveforms for a regolith target; specified impact force is $6.1*10^5$ N. D) Power density spectra for each target material, bedrock (black), regolith (yellow), and cohesive sediments (yellow) for synthetics at the source (solid colors) and 10 km (dotted) from the source. Power spectra are calculated using the same parameters as in Fig. 4. Viking 2 seismometer noise floor, SEIS-VBB, and SEIS-SP noise floors are indicated with broken lines. Synthetics

are low-pass filtered with a corner at 50 Hz. The synthetic seismogram waveforms used to generate these plots are available in the online supplement.

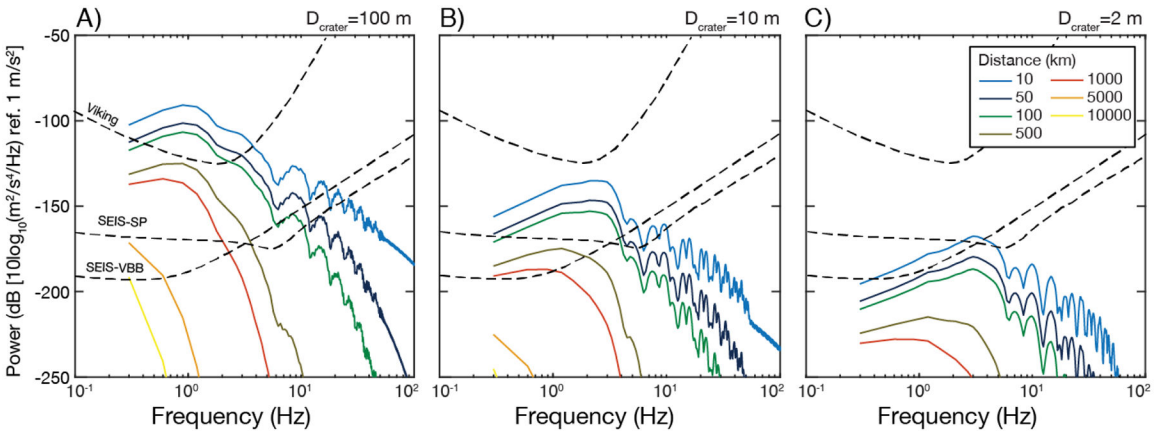

Figure 6.

Scaling of synthetic power spectra for the distance dependent effects of geometric spreading (Fig. 4c) and attenuation (see text) to couple the local 3-D simulations in WPP to global 1-D wave propagation in AxiSEM. Source parameters in this example are for a 6.5 km/s bolide hitting a cohesive sediment target with an impact angle of 45°. Only the vertical component of motion is shown. Power spectra are calculated using the same parameters as in Fig. 4. A) Results for a 100-meter diameter crater. B) Results for a 10-meter diameter crater. C) Results for a 2-meter diameter crater, and legend for distances. Frequencies below 0.8 Hz are not well-resolved in the 3-D model. As in Fig. 5, the Viking 2 seismometer noise floor, SEIS-VBB, and SEIS-SP noise floors are indicated with broken lines. Seismograms are low-pass filtered with a corner at 50 Hz. The synthetic seismogram waveforms used to generate these plots are available in the online supplement.

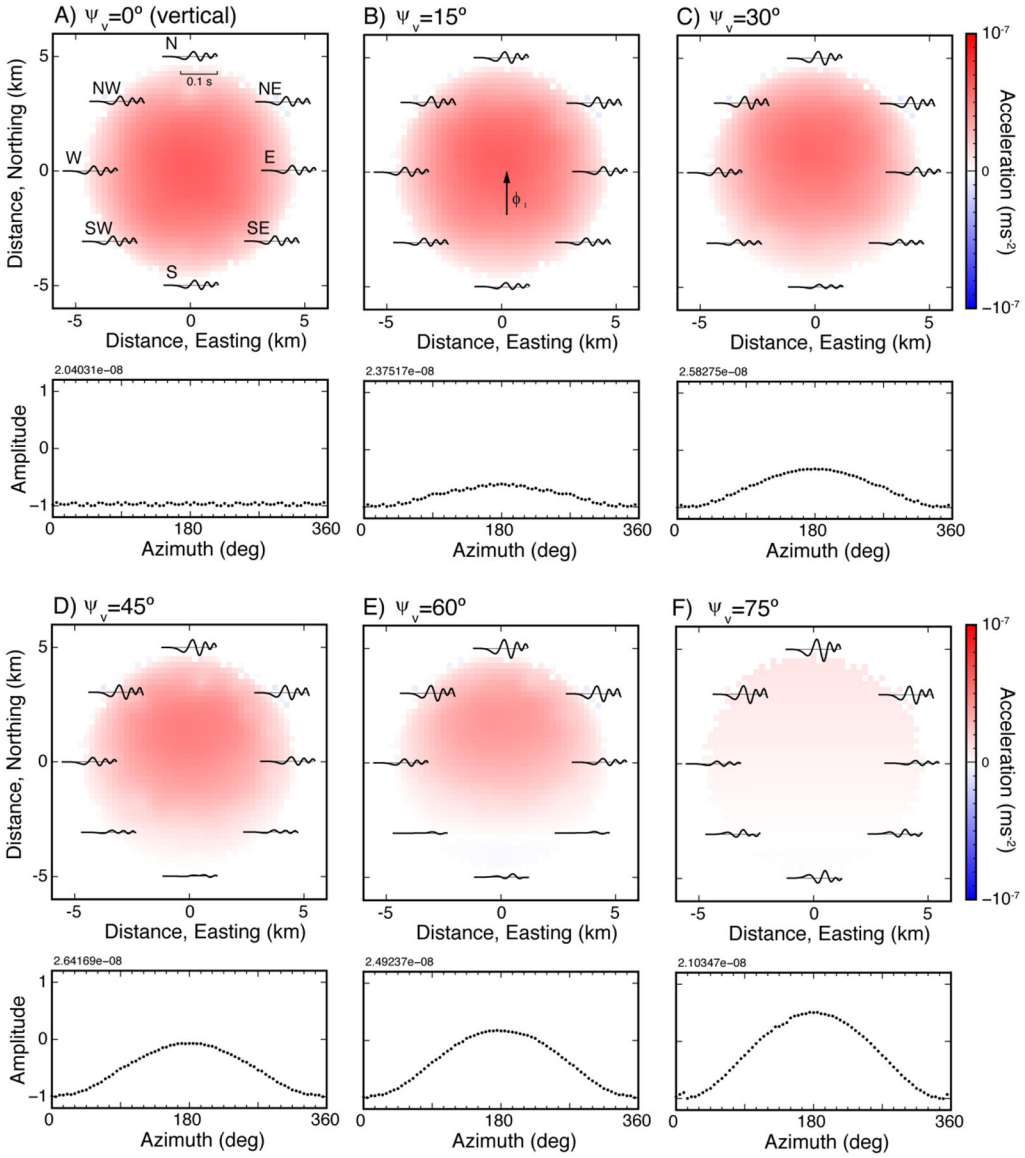

Figure 7.

Effect of impact angle, ψ_V on the radiation pattern of our impact source. In all cases, the specified impact azimuth is North (0°). Source parameters are for a 6.5 km/s bolide hitting a soft sediment target and a force resulting in a 10-meter diameter impact crater. In all cases, acceleration seismograms are measured for the polarity and amplitude on the vertical component of motion. Receivers are buried beneath the surface and distributed along the lower hemisphere of a 5 km radius sphere centered on the source at [0,0]. Surface stations are located every 1° on the perimeter of a 5 km radius circle centered on the source. The inset seismograms on the perimeter of each simulation are situated at the surface, and show the P-wave arrivals in a 0.15 s time window with time increasing to the right for every 45° azimuth. The relative amplitude at the P-wave of the surface receivers are shown in the plot underlying each radiation pattern. Note that a polarity reversal occurs for the stations at the free surface, so they are opposite in amplitude to the stations positioned at depth.

Amplitudes of these seismograms are normalized to the maximum amplitude shown in the panel underlying each plot. A) Radiation pattern for a vertical source ψ_V=0°. B) Radiation pattern for ψ_V=15°. C) Radiation pattern for ψ_V=30°. D) Radiation pattern for ψ_V=45°. E) Radiation pattern for ψ_V=60°. F) Radiation pattern for ψ_V=75°. The synthetic seismogram waveforms used to generate these plots are available in the online supplement.

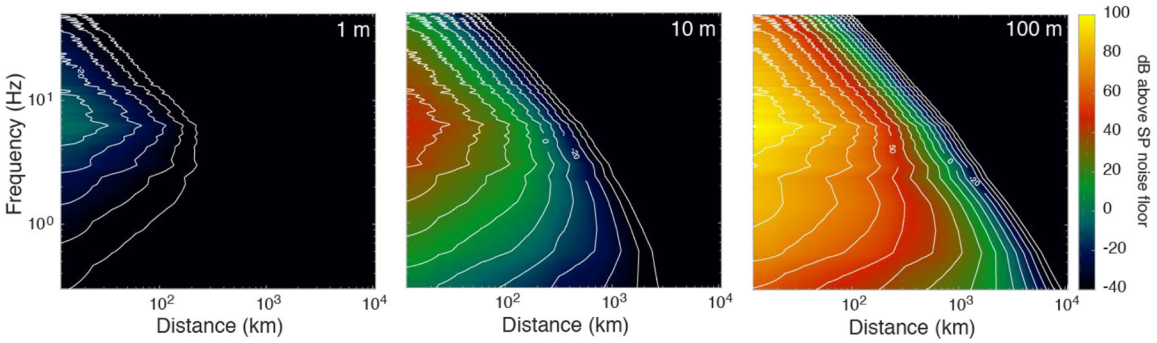

Figure 8.

Detectability of impacts of varying size above a reference noise floor of the SEIS SP seismic instrument on Mars. Source parameters are for a 6.5 km/s bolide hitting a soft sediment target and producing a crater with the diameter indicated in the upper right of each panel. The contour interval is 10 dB, with 0 dB referring to the noise floor of SEIS SP; all seismograms were low-pass filtered at 50 Hz prior to computing the power spectrum at each distance. Power spectra are calculated using the same parameters as in Fig. 4. The synthetic seismogram waveforms used to generate these plots are available in the online supplement.

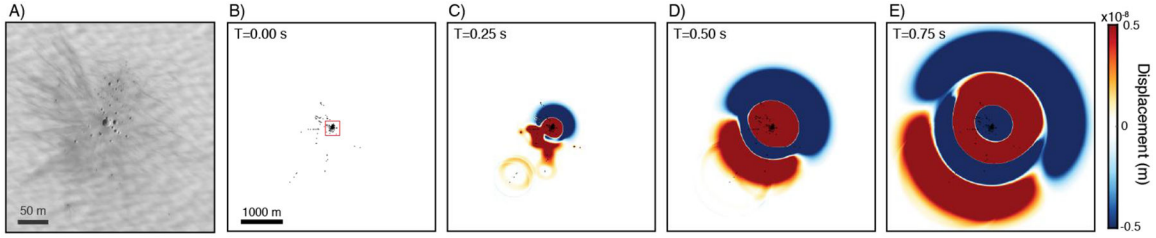

Figure 9.

Snapshots of the seismic wavefield for an impact cluster centered on longitude −125.759° and latitude −3.61615° (Site 11 in our database); synthetics are available in the online supplement. This impact cluster consists of >192 individual craters, with the largest crater having a diameter of 17.5 m. Using cluster geometry, we estimated an azimuth of 30.9° and impact angle of 55.3°. A) HiRISE image PSP_007036_1765 of the highlighted region. North is up. B) Vertical displacement snapshot situated on the cluster at the origin time of the simulation. Red box indicates the context for the image from part A. Each panel is a zoom on the central 5 km × 5 km region at the center of the 20 km × 20 km × 20 km simulation grid. Crater positions are marked in black. The time step of the simulation snapshot is indicated in the upper left. C-E) time steps into the simulation; ground displacement is scaled equally in all panels and is saturated on the color scale.

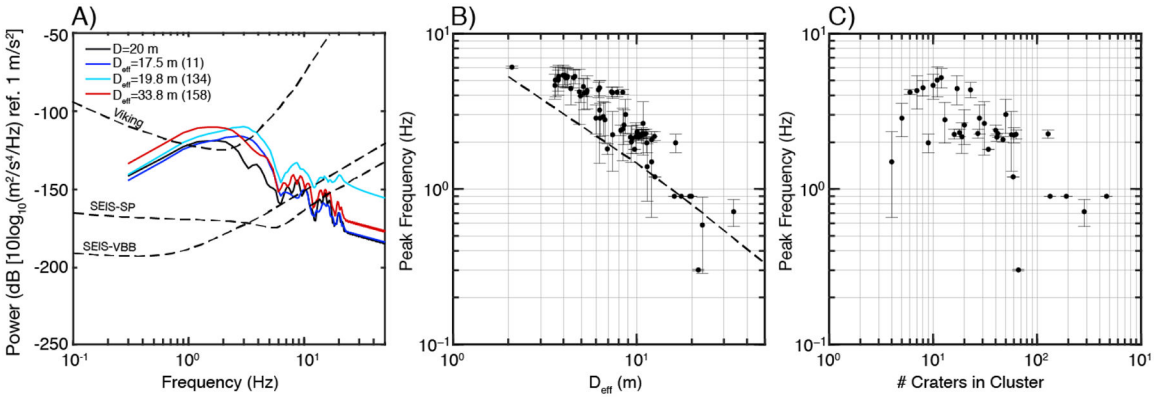

Figure 10.

Peak corner frequency measurements of martian impact clusters. A) Power spectra for a singular impact with a 20 m diameter, and power spectra for several impact clusters in our dataset with similar effective diameters. Power spectra are calculated for a source 10 km from the seismometer; for clusters we use the average location of the impact craters to determine the cluster center. As in Fig. 5, the Viking 2 seismometer noise floor, SEIS-VBB, and SEIS-SP noise floors are indicated with broken lines, and power spectra of each impact cluster is calculated using the same parameters as in Fig. 4. All seismograms were low-pass filtered at 50 Hz prior to computing the power spectrum. The cluster identifier in our database in (Daubar et al., 2019) is given in parentheses next to each effective crater diameter, and synthetic seismogram waveforms used to for each event are available in the online supplement. B) Peak corner frequencies measured at the point where the power spectrum falls below the SEIS-SP noise floor for impact clusters in our database. Dashed line is the measured corner frequency for singular impact events. C) Peak corner frequency as in (B) except against the number of craters identified in each cluster.

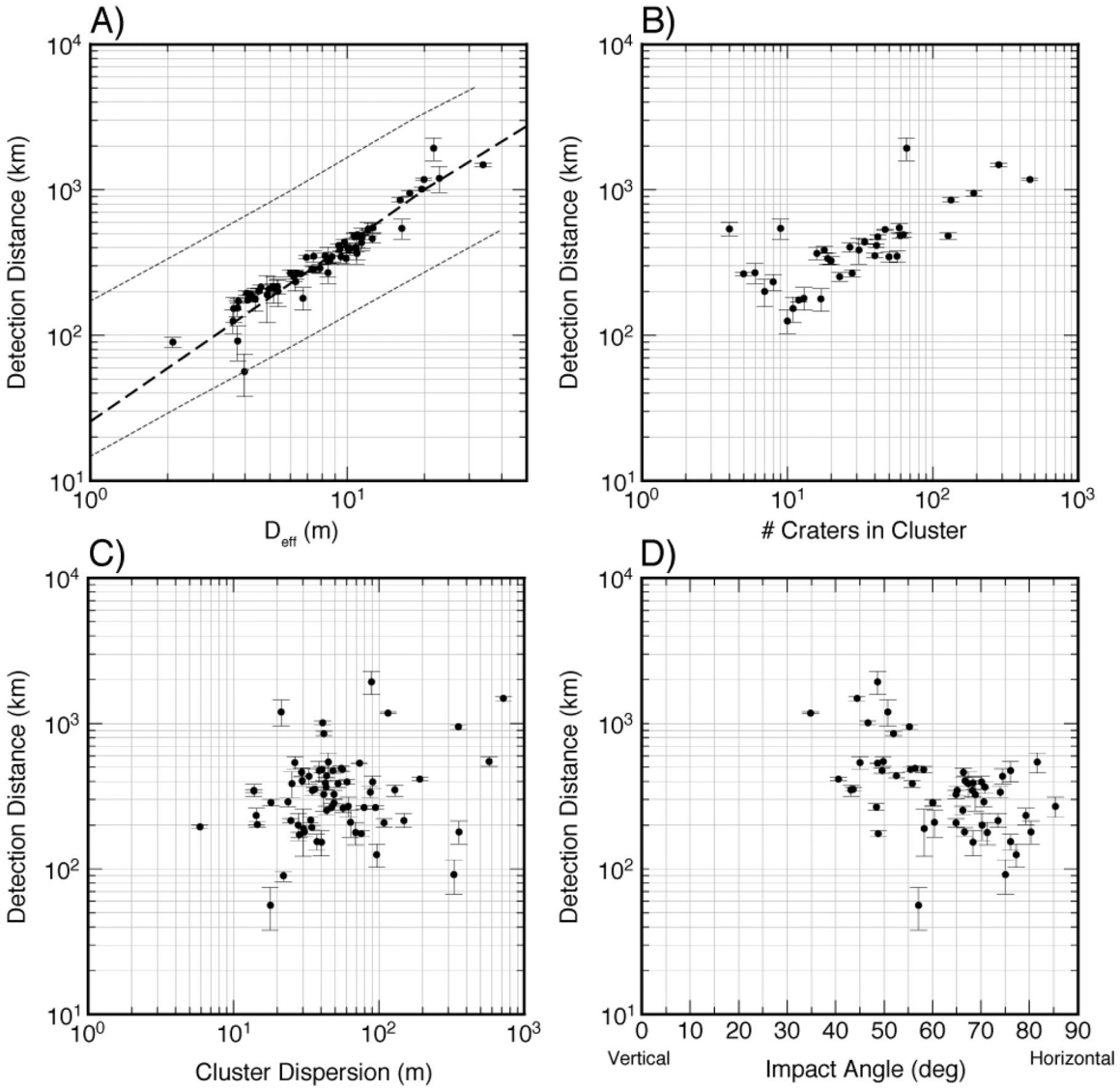

Figure 11.

Detectability of impact clusters in our martian crater database. Detectability is defined by the distance at which the distance- and attenuation-corrected power spectra of the impact cluster ceases to fall above the SEIS-SP noise floor (0 dB). A) The effective crater diameter calculated for each cluster against the maximum detectable distance of the cluster. Broken line is the maximum detectable distance for singular impacts. Dotted lines are the uncertainties in detectability of singular impacts from the analysis by (Teanby, 2015). B) The relationship between detectability and the number of individual craters in a cluster. C) The effect of cluster dispersion on detectability. D) The effect of impact angle (measured from the vertical) on cluster detectability.

Table 1.

Near Surface Material Properties

Target Material/Property	$\bar{Y}$ (MPa)	ρ (kg/m3)	V_p (m/s)	V_s (m/s)	V_p/V_s
Regolith	0.001	1500	1000	500	2.0
Cohesive Sediments	0.065	2100	4000	2000	2.0
Bedrock	10.00	3200	6000	3600	1.7